

Comparison of particle trajectories and collision operators for collisional transport in nonaxisymmetric plasmas

M Landreman,^{1,*} H M Smith,² A Mollén,³ and P Helander²

¹*Institute for Research in Electronics and Applied Physics,
University of Maryland, College Park, MD, 20742, USA*

²*Max-Planck-Institut für Plasmaphysik, 17491 Greifswald, Germany*

³*Department of Applied Physics, Nuclear Engineering,
Chalmers University of Technology and Euratom-VR Association, Göteborg, Sweden*

(Dated: February 5, 2014)

In this work, we test the validity of several common simplifying assumptions used in numerical neoclassical calculations for nonaxisymmetric plasmas. First, neoclassical phenomena are computed for the LHD and W7-X stellarators using several versions of the drift-kinetic equation, including the commonly used incompressible- $\mathbf{E} \times \mathbf{B}$ -drift approximation and two other variants, corresponding to different effective particle trajectories. It is found that for electric fields below roughly one third of the resonant value, the different formulations give nearly identical results, demonstrating the incompressible $\mathbf{E} \times \mathbf{B}$ -drift approximation is quite accurate in this regime. However, near the electric field resonance, the models yield substantially different results. We also compare results for various collision operators, including the full linearized Fokker-Planck operator. At low collisionality, the radial transport driven by radial gradients is nearly identical for the different operators, while in other cases it is found to be important that collisions conserve momentum.

I. INTRODUCTION

One important difference between axisymmetric and nonaxisymmetric plasmas is that neoclassical effects in the latter are more sensitive to small values of the radial electric field

*mattland@umd.edu

E_r . In axisymmetric plasmas, in order for the radial electric to modify the collisional ion heat flux and other neoclassical phenomena, the poloidal ion Mach number $(B/B_{\text{pol}})|\mathbf{v}_E|/v_i$ must approach ~ 1 , since an E_r of corresponding magnitude is required to modify the trapped region of phase space[1]. Here, B is the magnetic field magnitude, B_{pol} is the poloidal magnetic field, \mathbf{v}_E is the $\mathbf{E} \times \mathbf{B}$ drift, and $v_i = \sqrt{2T_i/m_i}$ is the ion thermal speed. However, in nonaxisymmetric plasmas, a much smaller value of E_r can modify the collisional fluxes [2–4]. The reason is that helically trapped particles experience a secular radial magnetic drift, and whichever process first interrupts this radial motion will thereby determine the step size for radial diffusion. When $E_r = 0$, the radial magnetic drift is interrupted by collisions, which cause the particle to gain parallel momentum and de-trap. But if E_r is sufficient for the poloidal $\mathbf{E} \times \mathbf{B}$ precession frequency to exceed the effective collisional detrapping rate, $\mathbf{E} \times \mathbf{B}$ precession begins to carry helically trapped particles onto untrapped trajectories, and also confines the trapped orbits by convecting them (usually poloidally) around the torus, thereby limiting the radial step size and transport. This transition from collisional ($1/\nu$ -regime) to E_r -limited ($\sqrt{\nu}$ -regime) transport typically occurs at values of E_r for which the poloidal Mach number is still $\ll 1$, due to the low collisionality in typical experiments. (Here, ν denotes a collision frequency.) For this reason, stellarator transport at low collisionality is sensitive to small values of E_r . A variety of codes have been developed to compute these neoclassical effects in stellarators [5–13].

However, including the physics of $\mathbf{E} \times \mathbf{B}$ precession in a δf drift-kinetic equation (or code to solve such an equation) is complicated by several issues. First, if a rigorous expansion in $\rho_* \ll 1$ is employed, $\mathbf{E} \times \mathbf{B}$ precession is formally excluded when the usual drift ordering $\mathbf{v}_E \sim \rho_* v_i$ is used, but the high-flow ordering $\mathbf{v}_E \sim v_i$ is not a useful ordering either, since it leads to contradictions in a general nonaxisymmetric field [14, 15]. Here, $\rho_* = \rho/L$ where ρ is the ion gyroradius and L is a typical macroscopic scale length. Second, if the \mathbf{v}_E poloidal precession term is included in a radially local, time-independent kinetic equation for δf (the departure of the distribution function from a Maxwellian), unphysical constraints are placed on the distribution function, as we will prove in section III by considering appropriate moments of the kinetic equation. These constraints only appear when $E_r \neq 0$, meaning a small but nonzero E_r is a singular perturbation of the $E_r = 0$ case. These unphysical behaviors have been eliminated in previous codes[4] by making the ad-hoc replacement $1/B^2 \rightarrow 1/\langle B^2 \rangle$ (where $\langle \dots \rangle$ denotes a flux surface average) in the $\mathbf{E} \times \mathbf{B}$ drift. At

the same time, variation in the particles' energy and pitch angle associated with E_r is neglected. These replacements and omissions are chosen so as to restore the variational form of the kinetic equation [5, 6]. These changes to the kinetic equation may be called the “incompressible- $\mathbf{E} \times \mathbf{B}$ -drift” approximation [16]. Some investigations have indicated that the incompressible- $\mathbf{E} \times \mathbf{B}$ -drift approximation may be reasonably accurate for small E_r but a poor approximation for larger E_r [16, 17]. This issue of which collisionless terms to include in the kinetic equation is effectively a choice between particle trajectories, since the collisionless guiding center trajectories are equivalent to the characteristic curves of the drift-kinetic equation.

Another limitation of many past stellarator neoclassical calculations is that they are often performed with simplified models for collisions. The linearized Fokker-Planck collision operator – the most accurate linear operator available – has been implemented in a variety of tokamak neoclassical codes [18–22]. However, due to the numerical challenge of the extra toroidal dimension in stellarators, many stellarator neoclassical codes retain only pitch-angle scattering collisions, so coupling in the energy dimension is eliminated. The pitch-angle scattering operator lacks the momentum conservation property of the Fokker-Planck operator, which is known to be important in many situations [23]. Several techniques have been devised and implemented [9, 24–26] to effectively restore momentum conservation by post-processing the transport coefficients obtained with a pure pitch-angle scattering operator, but these methods will not exactly reproduce calculations with the full linearized Fokker-Planck operator. The NEO-2 code has implemented the full linearized Fokker-Planck operator for stellarator geometry [10], but using a field-line-tracing method which makes it difficult to add the important effect of poloidal $\mathbf{E} \times \mathbf{B}$ precession.

Here, we describe a new stellarator neoclassical code SFINCS (the Stellarator Fokker-Planck Iterative Neoclassical Conservative Solver) that can be used to explore the aforementioned issues, comparing various models for effective particle trajectories and collisions. Although we use the terminology of “effective trajectories,” the code uses continuum rather than Monte Carlo algorithms. The code solves the 4D drift-kinetic equation for the distribution function, retaining coupling in 2 spatial independent variables (toroidal and poloidal angle) and 2 velocity independent variables (speed and pitch angle), but neglecting radial coupling. (For comparison, DKES [5, 6] is 3D since energy coupling is neglected, while FORTEC-3D [11, 12] is 5D since radial coupling is retained.) General nonaxisymmetric

nested flux surface geometry is allowed, one or more species may be included, and several models for collisions are available, including the full inter-species linearized Fokker-Planck operator. The incompressible- $\mathbf{E} \times \mathbf{B}$ -drift trajectories are implemented, as are several other options for trajectories that include the true $\mathbf{E} \times \mathbf{B}$ drift. As we shall demonstrate, retaining the true form of the $\mathbf{E} \times \mathbf{B}$ drift comes at a cost, requiring sources/sinks in the kinetic equation in order for the solutions to be well behaved. While all of the various options for the particle trajectories have disadvantages, SFINCS allows the three options to be compared. As we will show in several calculations for the LHD and W7-X stellarators, in many experimentally relevant cases, the transport matrix elements are nearly identical for the various choices of particle trajectories. However, differences between the trajectory models emerge when the radial electric field grows comparable to the “resonant” value.

In the following section, we motivate the form of the kinetic equation solved by SFINCS, and detail the three models for particle trajectories that will be compared. For several of the particle trajectory models, additional sources/sinks and constraints must be included in the system of equations for the equations to be well posed and for the solutions to be well behaved. These issues are explored in section III. Details of the numerical implementation are given in section IV. Some of the numerical results presented are given in terms of a transport matrix, which is defined in section V. The numerical results are presented in sections VI and VII, in which we discuss the transport matrix elements for the geometries of the LHD and W7-X stellarators, comparing a variety of assumptions about the particle trajectories and collision operator. In section VIII we discuss the results and conclude.

II. KINETIC EQUATIONS

We begin with the drift-kinetic equation (19) of Ref. [27]. The standard drift ordering is applied at first: $\rho_{*a} \ll 1$ where $\rho_{*a} = \rho_a/L$, $\mathbf{v}_E/v_a \sim \rho_{*a}$, $\partial/\partial t \sim \rho_{*a}^2 v_a/L$, and $\nu_a \sim v_a/L$. Here, $v_a = \sqrt{2T_a/m_a}$ is the thermal speed of species a , T_a is the temperature, m_a is the mass, $\rho_a = v_a m_a c / (Z_a e B)$ is the gyroradius, Z_a is the species charge in units of the proton charge e , c is the speed of light, L is a typical scale length, and ν_a is a collision frequency. No expansion in mass ratios or charges is made. We expand the distribution function as $f_a = f_{a0} + f_{a1} + \dots$. The leading order distribution function f_{a0} is taken to be a Maxwellian that is constant on

flux surfaces when expressed in terms of total energy $W_a = v^2/2 + Z_a e \Phi / m_a$:

$$f_{a0} = \eta_a(\psi) \left[\frac{m_a}{2\pi T_a(\psi)} \right]^{3/2} \exp \left(-\frac{m_a W_a}{T_a(\psi)} \right). \quad (1)$$

Here, Φ is the electrostatic potential and v is the speed. The mean flow of this Maxwellian is taken to be zero since, as argued in Refs. [14, 15], sonic flows are not permitted in a general stellarator. Taking $f_{a1}/f_{a0} \sim \rho_{*a}$, the terms of order $\sim \rho_{*a}(v/L)f_{a0}$ in (19) of Ref. [27] are then

$$v_{\parallel} \mathbf{b} \cdot (\nabla f_{a1})_{W_a, \mu} - C_a = -(\mathbf{v}_{ma} + \mathbf{v}_E) \cdot \nabla \psi \left(\frac{\partial f_{a0}}{\partial \psi} \right)_{W_a} + \frac{Z_a e}{m_a c} v_{\parallel} \mathbf{b} \cdot \frac{\partial \mathbf{A}}{\partial t} \frac{\partial f_{a0}}{\partial W_a} \quad (2)$$

where the radial magnetic drift is

$$\mathbf{v}_{ma} \cdot \nabla \psi = \frac{m_a c v_{\parallel}^2}{Z_a e B} \mathbf{b} \times (\mathbf{b} \cdot \nabla \mathbf{b}) \cdot \nabla \psi + \frac{m_a c v_{\perp}^2}{2 Z_a e B^2} \mathbf{b} \times \nabla B \cdot \nabla \psi = \frac{m_a c}{2 Z_a e B^2} \left(v_{\parallel}^2 + \frac{v_{\perp}^2}{2} \right) \mathbf{b} \times \nabla B \cdot \nabla \psi \quad (3)$$

(exactly true for any β in a magnetic equilibrium with isotropic pressure) and the $\mathbf{E} \times \mathbf{B}$ drift is $\mathbf{v}_E = (c/B^2) \mathbf{B} \times \nabla \Phi$. Here, $\mathbf{b} = \mathbf{B}/B$ is the unit vector along the magnetic field, v_{\parallel} and v_{\perp} denote the components of velocity parallel and perpendicular to \mathbf{B} , $2\pi\psi$ is the toroidal flux, \mathbf{A} is the magnetic vector potential, and C_a is the collision term for species a , linearized about the Maxwellians (1). Subscripts on gradients and partial derivatives indicate the quantities held fixed, and $\mu = v_{\perp}^2/(2B)$ is the magnetic moment.

Unfortunately, (2) does not contain the physics of $\mathbf{E} \times \mathbf{B}$ precession, since the characteristic curves of this equation correspond only to motion along the magnetic field lines. Consequently, important transport regimes such as the $\sqrt{\nu}$ regime cannot be obtained using (2). To retain $\mathbf{E} \times \mathbf{B}$ precession, we also keep the term $(\mathbf{v}_E + \mathbf{v}_{ma}) \cdot \nabla f_{a1}$ in (2), even though according to the formal ordering it should appear at next order. A similar step is made in other stellarator neoclassical calculations [5, 6]. The mathematical reason why this term is important at low collisionality is that it has different symmetry properties than other, possibly larger, terms in (2). For instance, it survives if a bounce average is used to annihilate the first term. (We will not bounce average the kinetic equation here, but when the collisionality is low, the solution of the full equation becomes asymptotically close to the solution of the bounce-averaged equation.)

As shown in Appendix C of Ref. [28], we may choose the gauge for the electromagnetic potentials such that $-c^{-1} \mathbf{b} \cdot \partial \mathbf{A} / \partial t = \langle E_{\parallel} B \rangle / \langle B^2 \rangle$ on the right-hand side of (2). Here,

angle brackets denote a flux surface average:

$$\langle \dots \rangle = \frac{1}{V'} \int_0^{2\pi} d\theta \int_0^{2\pi} d\zeta \frac{(\dots)}{\mathbf{B} \cdot \nabla \zeta} \quad (4)$$

where $V' = \int_0^{2\pi} d\theta \int_0^{2\pi} d\zeta / \mathbf{B} \cdot \nabla \zeta$, θ and ζ are poloidal and toroidal magnetic angles satisfying

$$\mathbf{B} = \nabla \psi \times \nabla \theta + \iota \nabla \zeta \times \nabla \psi, \quad (5)$$

$\iota = 1/q$ is the rotational transform, and q is the safety factor. Thus, (2) becomes

$$(v_{\parallel} \mathbf{b} + \mathbf{v}_E + \mathbf{v}_{ma}) \cdot (\nabla f_{a1})_{W_a, \mu} - C_a = -(\mathbf{v}_{ma} + \mathbf{v}_E) \cdot \nabla \psi \left(\frac{\partial f_{a0}}{\partial \psi} \right)_{W_a} + \frac{Z_a e}{T_a} v_{\parallel} \frac{B \langle E_{\parallel} B \rangle}{\langle B^2 \rangle} f_{a0}. \quad (6)$$

Even if the radial electric field is considered an input, this form of the kinetic equation remains nonlinear in the unknowns since the ∇f_{a1} term depends on the variation of Φ on a flux surface, and this variation is an unknown like f_{a1} .

To make the problem linear, we make use of the fact that the electrostatic potential is nearly a flux function. We define $\Phi_0 = \langle \Phi \rangle$ and $\Phi_1 = \Phi - \Phi_0$. We assume $\Phi_1 \ll \Phi_0$, and we will show shortly that this assumption is self-consistent. Since $e\Phi_0/T_a \sim 1$ in the drift ordering, then $e\Phi_1/T_a \ll 1$. We do not expand in the ion charge Z_a . Equation (1) then gives $f_{a0} \approx F_a [1 - Z_a e \Phi_1 / T_a]$ where

$$F_a = n_a(\psi) \left[\frac{m_a}{2\pi T_a(\psi)} \right]^{3/2} \exp \left(-\frac{m_a v^2}{2T_a(\psi)} \right) \quad (7)$$

and $n_a = \eta_a \exp(-Z_a e \Phi_0 / T_a)$ is the leading order density. We define the leading-order total energy $W_{a0} = v^2/2 + Z_a e \Phi_0 / m_a$, and leading-order $\mathbf{E} \times \mathbf{B}$ drift $\mathbf{v}_{E0} = (c/B^2)(d\Phi_0/d\psi)\mathbf{B} \times \nabla \psi$. As the relative differences between f_{a0} and F_a , between W_a and W_{a0} , and between \mathbf{v}_E and \mathbf{v}_{E0} are all small, we may replace the former quantities with the latter ones in (6). At the same time, we note

$$\frac{\mathbf{v}_E \cdot \nabla \psi}{\mathbf{v}_{ma} \cdot \nabla \psi} \sim \frac{1}{\epsilon} \frac{Z_a e \Phi_1}{T_a} \quad (8)$$

where ϵ is the relative variation of B on a flux surface, and taking the ratio (8) to be small, the $\mathbf{v}_E \cdot \nabla \psi$ term in (6) may be neglected. Thus, we obtain

$$(v_{\parallel} \mathbf{b} + \mathbf{v}_{E0} + \mathbf{v}_{ma}) \cdot (\nabla f_{a1})_{W_{a0}, \mu} - C_a = -(\mathbf{v}_{ma} \cdot \nabla \psi) \left(\frac{\partial F_a}{\partial \psi} \right)_{W_{a0}} + \frac{Z_a e}{T_a} v_{\parallel} \frac{B \langle E_{\parallel} B \rangle}{\langle B^2 \rangle} F_a. \quad (9)$$

where C_a is now the collision operator linearized about F_a rather than f_{a0} ,

$$\left(\frac{\partial F_a}{\partial \psi} \right)_{W_{a0}} = \left[\frac{1}{p_a} \frac{dp_a}{d\psi} + \frac{Z_a e}{T_a} \frac{d\Phi_0}{d\psi} + \left(x_a^2 - \frac{5}{2} \right) \frac{1}{T_a} \frac{dT_a}{d\psi} \right] F_a, \quad (10)$$

and $x_a = v/v_a$. If F_a and Φ_0 are considered known, then (9) is now linear in the unknowns f_{a1} , and Φ_1 has decoupled from the kinetic equations.

We note that in some circumstances the ratio (8) may not be small [3], particularly for impurities [13] with $Z_a \gg 1$. However, treating the ratio (8) as finite leads to a kinetic equation that is nonlinear in the unknowns. We neglect these nonlinear effects of Φ_1 in the present linear study, but such effects will be important to examine in future work.

For numerical computations, it is convenient to use coordinates for which the ranges of allowed values are independent of the other coordinates. As W_{a0} and μ do not have this property, it is convenient to switch to coordinates x_a and $\xi = v_{||}/v$. Carrying out this change of variables on the first term of (9), we find

$$\dot{\mathbf{r}} \cdot (\nabla f_{a1})_{W_{a0}, \mu} = \dot{\mathbf{r}} \cdot (\nabla f_{a1})_{x_a, \xi} + \dot{x}_a \left(\frac{\partial f_{a1}}{\partial x_a} \right)_{\mathbf{r}, \xi} + \dot{\xi}_a \left(\frac{\partial f_{a1}}{\partial \xi} \right)_{\mathbf{r}, x_a}, \quad (11)$$

where \mathbf{r} denotes the position vector,

$$\dot{\mathbf{r}} = v_{||} \mathbf{b} + \mathbf{v}_{E0} + \mathbf{v}_{ma}, \quad (12)$$

$$\dot{x}_a = (\mathbf{v}_{ma} \cdot \nabla \psi) \left(-\frac{x_a}{2T_a} \frac{dT_a}{d\psi} - \frac{Z_a e}{2T_a x_a} \frac{d\Phi_0}{d\psi} \right), \quad (13)$$

and

$$\dot{\xi}_a = -\frac{1 - \xi^2}{2B\xi} v_{||} \mathbf{b} \cdot \nabla B + \xi(1 - \xi^2) \frac{c}{2B^3} \frac{d\Phi_0}{d\psi} \mathbf{B} \times \nabla \psi \cdot \nabla B - \frac{1 - \xi^2}{2B\xi} \mathbf{v}_{ma} \cdot \nabla B. \quad (14)$$

For the rest of this work, we will neglect the \mathbf{v}_{ma} term in (12), the $dT_a/d\psi$ term in (13), and the $\mathbf{v}_{ma} \cdot \nabla B$ term in (14), for several reasons. First, if the \mathbf{v}_{ma} term in (12) were retained, we would need to solve a 5D rather than 4D problem due to the radial coupling (i.e. ψ appearing as a derivative rather than merely as a parameter). Second, once radial coupling is dropped, we must also drop the $dT_a/d\psi$ term in (13) and the $\mathbf{v}_{ma} \cdot \nabla B$ term in (14) in order for μ to be conserved. Third, dropping these terms conveniently eliminates all dependence of the transport matrix (defined in section V) on $dT_a/d\psi$ and $dB/d\psi$. Fourth, we wish to focus on the effects of the radial electric field. The omitted terms may be important in other situations, but here our primary interest is the treatment of the $d\Phi_0/d\psi$ terms. Our kinetic equation then becomes

$$\dot{\mathbf{r}} \cdot (\nabla f_{a1})_{x_a, \xi} + \dot{x}_a \left(\frac{\partial f_{a1}}{\partial x_a} \right)_{\mathbf{r}, \xi} + \dot{\xi}_a \left(\frac{\partial f_{a1}}{\partial \xi} \right)_{\mathbf{r}, x_a} - C_a = -(\mathbf{v}_{ma} \cdot \nabla \psi) \left(\frac{\partial F_a}{\partial \psi} \right)_{W_{a0}} + \frac{Z_a e}{T_a} v_{||} \frac{B \langle E_{||} B \rangle}{\langle B^2 \rangle} F_a. \quad (15)$$

where the effective particle trajectory equations are

$$\begin{aligned}\dot{\mathbf{r}} &= v_{\parallel} \mathbf{b} + \frac{c}{B^2} \frac{d\Phi_0}{d\psi} \mathbf{B} \times \nabla\psi, \\ \dot{x}_a &= -(\mathbf{v}_{ma} \cdot \nabla\psi) \frac{Z_a e}{2T_a x_a} \frac{d\Phi_0}{d\psi}, \\ \dot{\xi}_a &= -\frac{1-\xi^2}{2B\xi} v_{\parallel} \mathbf{b} \cdot \nabla B + \xi(1-\xi^2) \frac{c}{2B^3} \frac{d\Phi_0}{d\psi} \mathbf{B} \times \nabla\psi \cdot \nabla B.\end{aligned}\tag{16}$$

We will refer to (16) as the “full trajectories.”

The $d\Phi_0/d\psi$ terms in \dot{x}_a and $\dot{\xi}_a$ may be interpreted as a finite orbit width effect. As a particle drifts radially, it experiences a varying electrostatic potential (even if the potential is a flux function.) Thus the potential energy of the particle changes, so to maintain a constant total energy, the kinetic energy must change at an equal and opposite rate, giving rise to the $d\Phi/d\psi$ term in \dot{x}_a . Then to conserve μ while v changes, ξ must also change appropriately, giving rise to the $d\Phi_0/d\psi$ term in $\dot{\xi}_a$. Without these $d\Phi_0/d\psi$ terms in \dot{x}_a and $\dot{\xi}_a$, μ will not be conserved, whereas you can verify that μ is indeed conserved by (16). Note that the $d\Phi_0/d\psi$ term in $\dot{\mathbf{r}}$ is the same order in the ρ_* expansion as the $d\Phi_0/d\psi$ terms in \dot{x}_a and $\dot{\xi}_a$, suggesting that if the former term is retained, the latter terms should be retained as well.

A large number of stellarator neoclassical codes [4–6] effectively solve (15) with the alternative trajectory equations

$$\begin{aligned}\dot{\mathbf{r}} &= v_{\parallel} \mathbf{b} + \frac{c}{\langle B^2 \rangle} \frac{d\Phi_0}{d\psi} \mathbf{B} \times \nabla\psi, \\ \dot{x}_a &= 0, \\ \dot{\xi}_a &= -\frac{1-\xi^2}{2B\xi} v_{\parallel} \mathbf{b} \cdot \nabla B.\end{aligned}\tag{17}$$

We refer to these equations as the “DKES trajectories,” in light of their use in the widely applied code DKES [5, 6]. These trajectories differ from (16) both in the neglect of the $d\Phi_0/d\psi$ terms in \dot{x}_a and $\dot{\xi}_a$, and in the replacement $B^2 \rightarrow \langle B^2 \rangle$ in $\dot{\mathbf{r}}$. The motivation for approximating the $\mathbf{E} \times \mathbf{B}$ drift in this manner will be clarified in section III. As shown in Refs. [17, 29], in a symmetric magnetic field, the model (17) possesses a conserved quantity which is equal to μ when $d\Phi_0/d\psi = 0$ but which differs from μ when $d\Phi_0/d\psi \neq 0$.

For comparison, we will also consider the following set of trajectory equations:

$$\begin{aligned}\dot{\mathbf{r}} &= v_{\parallel} \mathbf{b} + \frac{c}{B^2} \frac{d\Phi_0}{d\psi} \mathbf{B} \times \nabla\psi, \\ \dot{x}_a &= 0, \\ \dot{\xi}_a &= -\frac{1-\xi^2}{2B\xi} v_{\parallel} \mathbf{b} \cdot \nabla B\end{aligned}\tag{18}$$

which will be referred to as the “partial trajectories.” Equations (18) represent an intermediate step between (17) and (16), in that (18) includes the correct $\mathbf{E} \times \mathbf{B}$ drift, but not the $d\Phi_0/d\psi$ terms in \dot{x}_a and $\dot{\xi}_a$ required to conserve μ .

For all three trajectory models, the quasineutrality equation is effectively decoupled from the kinetic equation (15). At leading order, quasineutrality implies $\sum_a Z_a n_a = 0$. At next order, noting that both f_{a0} and f_{a1} contribute to density variation on a flux surface,

$$\sum_a \left(-\frac{Z_a^2 e \Phi_1}{T_a} n_a + Z_a \int d^3v f_{a1} \right) = 0.\tag{19}$$

This equation may be solved for Φ_1 , giving the variation of the potential on a flux surface. It follows that $e\Phi_1/T_a \sim f_{a1}/f_{a0} \sim \rho_{*a}$, so our earlier assumption that $e\Phi_1/T_a \ll 1$ is self-consistent.

Several choices can be made for the collision operator. The most accurate linear option is the Fokker-Planck operator [30, 31] linearized about the Maxwellians: $C_a = \sum_b C_{ab}^\ell$, where $C_{ab}^\ell = C_{ab}\{f_{a1}, F_b\} + C_{ab}\{F_a, f_{b1}\}$ and C_{ab} is the full bilinear Fokker-Planck operator between species a and b . This linearized operator may be written in many forms, and for numerical implementation, we find it convenient to use the form detailed in equations (14)-(16) of Ref. [22].

A simpler option used in many codes is the pitch-angle scattering operator [4]. This operator lacks several properties of the linearized Fokker-Planck operator, such as the momentum conservation property $\int d^3v v_{\parallel} C_{aa}^\ell = 0$. Several more accurate approximate operators have been used in the literature. One such operator we will consider later consists of the pitch-angle scattering operator plus an ad-hoc momentum-restoring term, given for the case of self-collisions by eq (3.69) in Ref. [31].

III. CONSERVATION PROPERTIES AND SOURCES

If one attempts to solve the kinetic equation (15) numerically using either the full or partial trajectories and $E_r \neq 0$, unphysical results will be obtained, with the numerical

solution not converging as resolution parameters are increased. We now explore the reason for this behavior. We will then describe a modified form of the kinetic equation which robustly produces more sensible results.

Consider the result of applying the operation

$$\left\langle \int d^3v (\dots) \right\rangle \quad (20)$$

to the kinetic equation (15) for each of the trajectory models (16)-(18). This operation annihilates the streaming and mirror terms, the collision operator, and the inhomogeneous drive terms. The operation (20) effectively produces a flux-surface-averaged mass conservation equation for each model. For the full trajectories and DKES trajectories, the $d\Phi_0/d\psi$ terms are also annihilated by (20), so the resulting mass conservation equation is just $0 = 0$. However, for the partial trajectories, the $d\Phi_0/d\psi$ term ($\mathbf{v}_{E0} \cdot \nabla f_{a1}$) is not annihilated by (20), leaving

$$c \left\langle \frac{1}{B^2} \mathbf{B} \times \nabla \psi \cdot \nabla \int d^3v f_{a1} \right\rangle \frac{d\Phi_0}{d\psi} = 0. \quad (21)$$

Thus, a nonzero $d\Phi_0/d\psi$ gives a singular perturbation to the $d\Phi_0/d\psi = 0$ limit in this partial trajectory model: the $d\Phi_0/d\psi = 0$ solution for f_{a1} need not satisfy $\langle (1/B^2) \mathbf{B} \times \nabla \psi \cdot \nabla \int d^3v f_{a1} \rangle = 0$, so f_{a1} must change dramatically as E_r is raised from 0 to a small nonzero value, a behavior which is unphysical. When $d\Phi_0/d\psi \neq 0$, (21) constrains f_{a1} in an unphysical manner, for there is no analogue to (21) in the more accurate averaged fluid mass conservation equation $0 = \langle \partial N_a / \partial t + \nabla \cdot (N_a \mathbf{V}_a) \rangle$ (i.e. the moment of the full Fokker-Planck equation with no expansion in ρ_* or other parameters), where N_a and \mathbf{V}_a are the full fluid density and velocity. The unphysical nature of (21) can also be seen from the fact that when the $d\Phi_0/d\psi$ terms in \dot{x}_a and $\dot{\xi}_a$ are retained in the more accurate trajectories (16), these terms precisely cancel (21).

Similarly, we can obtain an averaged energy conservation equation for each trajectory model by applying the operation

$$\sum_a \left\langle \int d^3v \frac{m_a v^2}{2} (\dots) \right\rangle \quad (22)$$

to (15). Again, the result is $0 = 0$ for the DKES trajectories. However, this time both the full and partial trajectory models give nonzero results: the partial trajectories give

$$c \sum_a \left\langle \frac{1}{B^2} \mathbf{B} \times \nabla \psi \cdot \nabla \int d^3v \frac{m_a v^2}{2} f_{a1} \right\rangle \frac{d\Phi_0}{d\psi} = 0. \quad (23)$$

and the full trajectories give

$$-c \sum_a \left\langle \frac{1}{B^2} \mathbf{B} \times \nabla \psi \cdot \nabla \int d^3v \frac{m_a v^2}{2} \frac{(1 + \xi^2)}{2} f_{a1} \right\rangle \frac{d\Phi_0}{d\psi} = 0. \quad (24)$$

The quantity multiplying $d\Phi_0/d\psi$ in (24) is proportional to the radial current $\sum_a Z_a \langle \int d^3v f_{a1} \mathbf{v}_{ma} \cdot \nabla \psi \rangle$, so it vanishes naturally when E_r is at the ambipolar value. However, as the radial current would usually not be zero when $E_r = 0$, (24) again implies a small nonzero E_r would be a singular perturbation of the $E_r = 0$ limit.

One motivation for use of the DKES trajectory model is now apparent: it is the only model that avoids the imposition of one or more unphysical constraints on the distribution function when $d\Phi_0/d\psi \neq 0$, constraints which cause an $E_r \neq 0$ calculation to be a singular perturbation of an $E_r = 0$ calculation.

The aforementioned problems with the partial and full trajectory models may be eliminated in the following manner. The kinetic equation becomes well behaved if we introduce small particle and heat sources

$$S_a(\psi, v) = S_{ap}(\psi) F_a(\psi, v) \left[x_a^2 - \frac{5}{2} \right] + S_{ah}(\psi) F_a(\psi, v) \left[x_a^2 - \frac{3}{2} \right] \quad (25)$$

where S_{ap} and S_{ah} are considered to be unknowns. (The factors involving x_a^2 in (25) are chosen so S_{ap} provides a particle source but no heat source, while S_{ah} provides a heat source but no particle source.) As these two new unknowns are now included in the system of equations on each flux surface, we must supply an equal number of additional constraints. The constraints we supply are $\langle \int d^3v f_{a1} \rangle = 0$ and $\langle \int d^3v v^2 f_{a1} \rangle = 0$, the sensible requirements that all the flux-surface-averaged density and pressure reside in F_a rather than f_{a1} . This method of modifying the system of equations has the added benefit (even in the $d\Phi_0/d\psi = 0$ limit) of eliminating the null solutions $f_{a1} = F_a$ and $f_{a1} = F_a v^2$. When S_a is included in the kinetic equation, new terms proportional to S_{ap} and/or S_{ah} now appear in the mass and energy conservation equations such as (21)-(24). These conservation equations imply that when $d\Phi_0/d\psi = 0$, S_{ap} and S_{ah} must vanish. However, now when $d\Phi_0/d\psi$ is increased from 0 to a small finite number, the sources can turn on to satisfy (21)-(24), eliminating the singular perturbation in f_{a1} . We find that numerical results are then well behaved, converging appropriately as numerical resolution parameters are increased, and smoothly going to the $E_r = 0$ results as E_r is decreased.

We do not claim that the method proposed here is an ideal solution: the sources (25) are ad-hoc and are not derived rigorously. However, by the techniques proposed here, we

can at least compare the three different trajectory models, and for most experimentally relevant values of E_r , we will show that the three models give nearly identical results. As already mentioned, the need for source terms disappears when the radial electric field equals the value required for ambipolarity, so the source terms do not interfere with the aim of eventually calculating the actual plasma transport.

The aforementioned mass and energy sources and constraints work when the Fokker-Planck collision operator is used, but not when the pure pitch-angle scattering or momentum-conserving model collision operator is used, since in these cases the kinetic equation has a larger null space (any function of v is a solution.) For these collision operators, we instead allow a general source $S_a(\psi, v)$, introducing N_x unknowns on each flux surface, where N_x is the number of grid points in v . To supply an equal number of constraints, we impose the equations $\left\langle \int_{-1}^1 d\xi f_{a1} \right\rangle = 0$ at each grid point in v .

IV. NUMERICAL IMPLEMENTATION

The SFINCS code solves the drift-kinetic equation (15) with (25) for the three trajectory models (16)-(18), for general nonaxisymmetric nested flux surface geometry, and for an arbitrary number of species. SFINCS is based on the Fokker-Planck code described in Ref. [22], generalized to allow nonaxisymmetry. SFINCS is also closely related to the radially global Fokker-Planck code for tokamaks described in Ref. [32]. Briefly, the kinetic equation is discretized using finite differences with a 5-point stencil in θ and ζ , using a truncated Legendre modal expansion in ξ , and using a spectral collocation method in x_a . The time-independent kinetic equation is solved directly (by solving a single sparse linear system), so the rate of convergence is not limited by the timescale of physical relaxation. The modifications compared to the code of Ref. [22] are the following. (1) f_{a1} , B , and other geometric operators are allowed to depend on the toroidal angle ζ , and the numerical grid is expanded to include this new coordinate. (2) The additional $d\Phi_0/d\psi$ terms in $\dot{\mathbf{r}}_a$, \dot{x}_a , and $\dot{\xi}_a$ are included. (3) The additional collision operators discussed above are included. (4) The extra constraint equations and sources are implemented as in (19) of Ref. [32]. Specifically, considering first the case of a single species for simplicity, the linear system has the block

structure

$$\begin{aligned} \text{Kinetic equation } \{ \begin{pmatrix} M_{11} & M_{12} & M_{13} \\ M_{21} & 0 & 0 \\ M_{31} & 0 & 0 \end{pmatrix} \underbrace{\begin{pmatrix} f_{a1} \\ S_{ap} \\ S_{ah} \end{pmatrix}}_{\text{Vector of unknowns}} &= \begin{pmatrix} R \\ 0 \\ 0 \end{pmatrix}, \end{aligned} \quad (26)$$

where R is the inhomogeneous term (i.e. the right-hand side) from (15), and the M operators are as follows: M_{11} represents the operator on the left-hand side of (15), M_{12} and M_{13} represent the S_{ap} and S_{ah} terms in (25) respectively, and M_{21} and M_{31} represent the aforementioned extra constraint equations introduced. For the case of multiple particle species, the linear system consists of blocks of the form (26) for each species, with coupling between species only through the collision operators in the M_{11} blocks.

The resulting large sparse linear system is solved using the PETSc[33, 34] library. A preconditioned iterative Krylov solver is employed, either GMRES[35] or BICGSTab(l)[36]. An effective preconditioner is typically obtained by dropping all coupling in the x_a coordinate, either for all Legendre modes in ξ , or for all but the first one or two Legendre modes. The preconditioner is LU -factorized directly using the SuperLU-dist[37, 38] package.

Note that poloidal and toroidal magnetic drifts could be included in the kinetic equation without increasing the density of the matrix, i.e. without increasing the computational expense of the method here. However, to include radial drifts acting on f_{a1} , the number of independent variables would increase from 4 to 5 since different flux surfaces would couple. This increase in dimensionality would be numerically challenging.

The magnetic geometry is specified in Boozer coordinates θ and ζ , in which

$$\mathbf{B} = \beta(\psi, \theta, \zeta) \nabla \psi + I(\psi) \nabla \theta + G(\psi) \nabla \zeta. \quad (27)$$

Here, $cI/2$ is the toroidal current inside the flux surface, and $cG/2$ is the poloidal current outside the flux surface. The geometric operators needed in the kinetic equation are then

$$\mathbf{B} \cdot \nabla X = \left(\iota \frac{\partial X}{\partial \theta} + \frac{\partial X}{\partial \zeta} \right) \mathbf{B} \cdot \nabla \zeta \quad (28)$$

and

$$\mathbf{B} \times \nabla \psi \cdot \nabla X = \left(G \frac{\partial X}{\partial \theta} - I \frac{\partial X}{\partial \zeta} \right) \mathbf{B} \cdot \nabla \zeta \quad (29)$$

where X can be any scalar quantity, and the inverse coordinate Jacobian is $\mathbf{B} \cdot \nabla \zeta = B^2/(G + \iota I)$. Thus, the magnetic geometry enters the kinetic equation only through the quantities I , G , ι , and $B(\theta, \zeta)$.

V. ION TRANSPORT MATRIX

We will present results of the numerical calculations in terms of the transport matrix L_{jk} , defined as follows:

$$\begin{pmatrix} \frac{Ze(G+\iota I)}{ncTG} \left\langle \int d^3v f \mathbf{v}_m \cdot \nabla \psi \right\rangle \\ \frac{Ze(G+\iota I)}{ncTG} \left\langle \int d^3v f \frac{mv^2}{2T} \mathbf{v}_m \cdot \nabla \psi \right\rangle \\ \frac{1}{v_i B_0} \langle BV_{\parallel} \rangle \end{pmatrix} = \begin{pmatrix} L_{11} & L_{12} & L_{13} \\ L_{21} & L_{22} & L_{23} \\ L_{31} & L_{32} & L_{33} \end{pmatrix} \begin{pmatrix} \frac{GTc}{ZeB_0v_i} \left[\frac{1}{n} \frac{dn}{d\psi} + \frac{Ze}{T} \frac{d\Phi}{d\psi} - \frac{3}{2T} \frac{dT}{d\psi} \right] \\ \frac{GTc}{ZeB_0v_i T} \frac{dT}{d\psi} \\ \frac{Ze}{T} (G + \iota I) \frac{\langle E_{\parallel} B \rangle}{\langle B^2 \rangle} \end{pmatrix} \quad (30)$$

Here, B_0 is the $(0,0)$ Fourier mode amplitude of $B(\theta, \zeta)$, and we have dropped i subscripts where possible to simplify the notation. When the DKES trajectories (17) are used, it can be shown that L_{jk} is symmetric for any value of E_r . When the trajectories (16) or (18) are used and $E_r = 0$, L_{jk} is symmetric as well. However, when the trajectories (16) or (18) are used and $E_r \neq 0$, the transport matrix defined in this manner is generally not symmetric.

Different definitions of the transport matrix have been given elsewhere in the literature [16], but the definition here has several nice properties. First, the matrix is dimensionless. Second, L_{jk} is symmetric (in the cases described above). Third, L_{jk} depends on the magnetic geometry and physical parameters only through B/B_0 , I/G , ι , a normalized collisionality

$$\nu' = \frac{(G + \iota I)\nu_{ii}}{v_i B_0}, \quad (31)$$

and a normalized electric field

$$E_* = \frac{cG}{\iota v_i B_0} \frac{d\Phi_0}{d\psi}, \quad (32)$$

and not on any other individual parameters such as density, temperature, G , etc. In (31), $\nu_{ii} = 4\sqrt{2\pi n} Z^4 e^4 \ln \Lambda / (3m^{1/2} T^{3/2})$ is the ion-ion collision frequency. Typically, $I \ll G$ and $G \approx B_0 R$ where R is the major radius of the device, so $\nu' \approx \nu_{ii} R / v_i$. In axisymmetry, E_* corresponds to the poloidal Mach number: $E_* \approx (B/B_{\text{pol}}) |\mathbf{v}_{E0}| / v_i$ where B_{pol} is the poloidal magnetic field. Therefore, E_* corresponds to the electric field normalized by the so-called resonant electric field [16] $E_r^{\text{res}} = r \nu v_i B / (Rc)$, with r/R the inverse aspect ratio.

Several properties of the matrix L_{jk} are noteworthy. Using the property $\int d^3v (g/F_i) C_{ii}\{g\} \leq 0$ for any g , which holds for all three ion-ion collision operators considered here, then $\text{sgn}(L_{11}) = \text{sgn}(L_{22}) = -\text{sgn}(L_{33}) = -\text{sgn}((G + \iota I)/B_0)$. This property holds when $E_r = 0$, and it holds when $E_r \neq 0$ for the DKES trajectories, but it may not hold when $E_r \neq 0$ for the partial or full trajectories. Second, for all three trajectory models, the

elements L_{jk} are independent of the sign of the electric field: $L_{jk}(E_*) = L_{jk}(-E_*)$, assuming the stellarator symmetry property $B(\theta, \zeta) = B(-\theta, -\zeta)$ for some choice of the origin of θ and ζ . This symmetry of L_{jk} follows from a symmetry in the kinetic equation: if the signs of θ , ζ , $v_{||}$, and $d\Phi_0/d\psi$ are all reversed in (15), the sign of f_{i1} will reverse, leaving the left-hand side of (30) unchanged.

VI. COMPARISON OF E_r TERMS

Figures (1) and (2) show a SFINCS computation of the ion transport matrix elements for the 3 trajectory models in two different stellarator geometries. The calculations in figure (1) are performed for the $r/a = 0.5$ surface of the LHD stellarator [39] in its standard configuration. (Here the flux function r is defined to be proportional to the square root of the toroidal flux enclosed by the flux surface in question.) The calculations in figure (2) are performed for the $r/a = 0.5$ surface of the W7-X stellarator [40, 41] in its standard configuration. In the LHD calculation, only the Boozer harmonics of $B(\theta, \zeta)/B_0$ with amplitude larger than 10^{-2} are retained, as listed in Table 1 of Ref. [4]. For both figures, the Fokker-Planck collision operator is used, and the collisionality is set to $\nu' = 0.01$. As both figures illustrate, the electric field has negligible effect on the transport matrix elements when $E_* < 0.01$. For these small values of the electric field, the radial step size for diffusion is limited by collisions rather than by $\mathbf{E} \times \mathbf{B}$ precession. As $E_r \rightarrow 0$, all the matrix elements converge smoothly to their $E_r = 0$ limits. For E_* in the range $[0.01, 0.3]$, the $\mathbf{E} \times \mathbf{B}$ precession suppresses radial transport, as can be seen by the reduction in $|L_{11}|$ and $|L_{22}|$. In this regime of E_* , the three trajectory models give nearly identical results for all the transport matrix elements. However, once E_* exceeds about 0.3, the results from the three trajectory models begin to separate.

In all probability, the reason why the three trajectory models agree so well with each other below the resonance is that they all capture the principal mechanism of transport in the $\sqrt{\nu}$ -regime. The $\mathbf{E} \times \mathbf{B}$ drift convects most locally trapped particles poloidally around the torus, thus preventing them from drifting to the wall, and the transport is instead dominated by shallowly trapped and barely passing particles that are scattered back and forth across the trapped-passing boundary on a time scale equal to the poloidal convection time [3]. This behavior is not likely to be affected by the approximations made in the DKES and partial

trajectory models.

In most plasma scenarios, E_* can be estimated by noting that the ambipolar electric field arises to bring the ion particle transport down to the electron level, and is therefore approximately determined so as to reduce the magnitude of the “thermodynamic force” appearing as the first component of the vector on the right-hand side of (30). The electric field is thus of order $E_r \sim T/(eL_\perp)$, where L_\perp denotes the length scale corresponding to the pressure gradient. It is thus expected that E_* is of order $E_* \sim \rho_\theta/L_\perp$, where $\rho_\theta = \rho/(\iota\epsilon)$, with ϵ the inverse aspect ratio. In W7-X, E_r is predicted to be particularly large in regions with steep density gradients and will in normal plasma scenarios stay below a few tens of kV/m, corresponding to E_* up to a few tenths[42]. In most of the plasma, E_* is however expected to be smaller than a few percent.

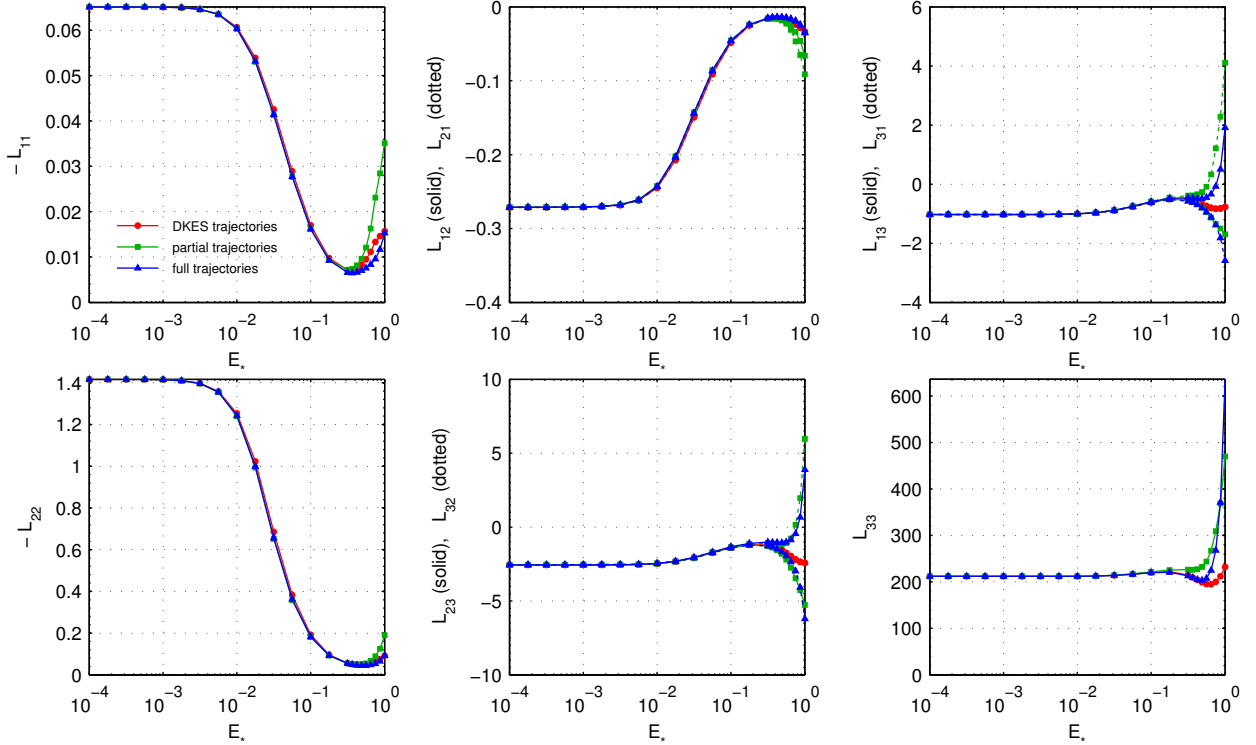


FIG. 1: (Color online) Comparison of trajectory models for LHD standard geometry at $\nu' = 0.01$, using linearized Fokker-Planck collisions. The ion transport matrix elements (defined in (30)) are plotted as functions of the normalized radial electric field (32).

Further analysis of whether the choice of trajectory model is significant in W7-X is shown in figure 3. This calculation is based on the scenario considered in figure 5 of Ref. [42]. We

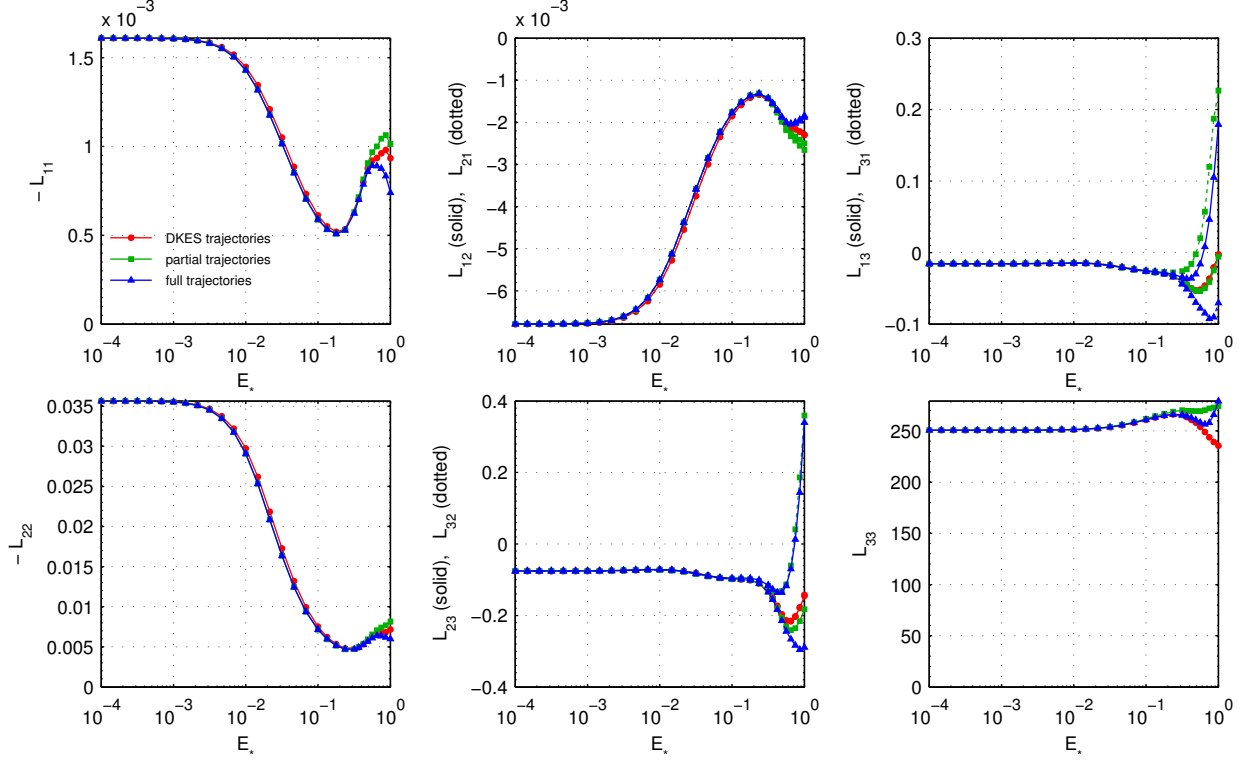


FIG. 2: (Color online) Comparison of trajectory models for W7-X standard geometry at $\nu' = 0.01$, using linearized Fokker-Planck collisions. The ion transport matrix elements (defined in (30)) are plotted as functions of the normalized radial electric field (32).

focus on the radial location $r = 0.45$ m ($r/a = 0.88$) in which the pressure gradient is strong. This gradient should result in a large E_r , as predicted both by the argument in the preceding paragraph, and by the modeling in Ref. [42] based on incompressible- $\mathbf{E} \times \mathbf{B}$ computations. (Here, the flux label r is defined by $\pi r^2 B_0 = 2\pi\psi$.) Matching the parameters in that work, we consider a pure hydrogen plasma with $n = 6.6 \times 10^{19} \text{ m}^{-3}$, $T_e = T_i = 1$ keV, $dn/dr = -1.2 \times 10^{21} \text{ m}^{-4}$, and $dT_e/dr = dT_i/dr = -16$ keV/m. These values correspond to $\nu' = 0.03$ and $E_r^{\text{res}} = 100$ kV/m. For this scenario, kinetic electrons are included in SFINCS along with the ions. Inter-species linearized Fokker-Planck collisions are included with no expansion in mass ratio.

The radial fluxes of ions and electrons as functions of E_r are shown in figure 3.A. The electron fluxes (dashed curves) are very small ($\sim \sqrt{m_e/m_i}$) compared to the ion fluxes and are identical between the three trajectory models. No difference between the models is expected for the electrons, since E_* defined using the electron rather than ion thermal speed

is always $\ll 1$. The vertical magenta dotted line indicates the ambipolar value of $E_r \approx 33$ kV/m, which is effectively identical for the three trajectory models, and comparable to the value predicted in [42]. This electric field is roughly one third of the resonant value, and therefore the ion transport coefficients are just beginning to separate for the three models. Heat fluxes are shown in figure 3.B, showing similar behavior to the particle fluxes.

Figure 3.C shows the surface-averaged ion parallel flow. At the ambipolar value of E_r , the three trajectory models yield similar values for the predicted flow. At lower magnitudes of E_r , the flows predicted by the three models are nearly indistinguishable. However, at larger electric fields, the three models begin to give quite different predictions. This change in behavior around $E_* \sim 0.3$ is consistent with the patterns in figures 1- 2. A similar pattern is visible in the bootstrap current density, shown in figure 3.D. At the ambipolar value of E_r , the partial trajectory model predicts 27% more bootstrap current than the full trajectory model, and the DKES model predicts 8% more bootstrap current than the full trajectory model. Interestingly, if the electric field exceeds 60 kV/m in the inward (ion root) direction, the bootstrap current in the full trajectory model changes sign, whereas there is no sign change in the DKES model.

VII. COMPARISON OF COLLISION OPERATORS

Figures (4)-(5) show the transport matrix elements for the LHD and W7-X geometries described earlier, this time comparing the different collision operators as a function of collisionality. The comparison is done for $d\Phi_0/d\psi = 0$, so the three trajectory models become identical, and the sources S_a vanish. It can be seen in the figures that at high collisionality, momentum conservation is important for all the transport matrix elements (with the possible exception of L_{22} .) At low collisionality, momentum conservation is unimportant for L_{11} , L_{12} , L_{21} , and L_{22} . These matrix elements represent $1/\nu$ -regime radial transport (when $\nu' \ll 1$), which is associated with pitch-angle scattering of helically trapped particles. Thus, the pitch-angle scattering approximation for collisions accurately captures the dominant physics in these cases. When $d\Phi_0/d\psi \neq 0$, the same is true for the $\sqrt{\nu}$ -regime, where the main effect of the collisions is to scatter particles across a thin collisional boundary layer in velocity space around the trapped-passing boundary.

The other matrix elements (L_{13} , L_{23} , L_{31} , L_{32} , and L_{33}) are more sensitive to momen-

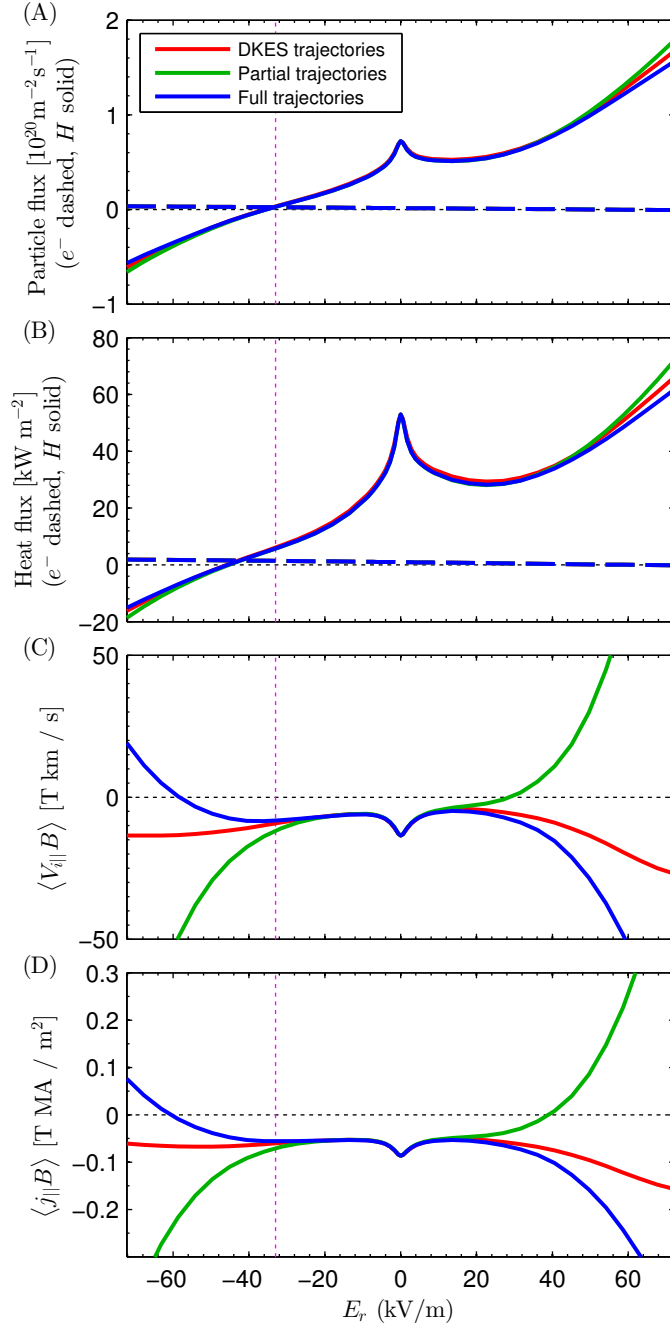


FIG. 3: (Color online) Fluxes and flows computed for a scenario of steep pressure gradient near the edge of W7-X. Magenta dotted line is the ambipolar E_r , effectively identical for the three trajectory models.

tum conservation at low collisionality. For all the matrix elements at all collisionalities, the momentum-conserving model operator reproduces all the trends of the more accurate linearized Fokker-Planck operator, though with some $O(1)$ differences.

Note in Figs. (4)-(5) that the scaling of the L_{11} and L_{12} coefficients at high collisionality depends crucially on whether momentum is conserved in the collision operator. In the momentum-conserving calculations, these transport coefficients are inversely proportional to ν , whereas they are proportional to ν if the collisions are approximated by pure pitch-angle scattering. To understand why, it is useful to recall that the Pfirsch-Schlüter particle flux consists of two terms: one related to the parallel friction force and one related to parallel viscosity [43, 44]. This is most easily seen by taking the scalar product of the lowest-order plasma current, which satisfies $\mathbf{J} \times \mathbf{B} = cp'(\psi)\nabla\psi$, with the momentum equation,

$$m_a n_a \mathbf{V}_a \cdot \nabla \mathbf{V}_a = n_a e_a (-\nabla\phi + c^{-1} \mathbf{V}_a \times \mathbf{B}) - \nabla p_a - \nabla \cdot \boldsymbol{\pi}_a + \mathbf{F}_a, \quad (33)$$

neglecting the left-hand side. Since $\nabla \cdot \mathbf{J} = 0$ and n_a is a flux function in lowest order, we obtain

$$\langle n_a \mathbf{V}_a \cdot \nabla \psi \rangle = \frac{1}{e_a p'(\psi)} \langle \mathbf{J} \cdot (\mathbf{F}_a - \nabla \cdot \boldsymbol{\pi}_a) \rangle, \quad (34)$$

where the term corresponding to the perpendicular component of the friction force \mathbf{F}_a represents the classical particle flux and the other terms the neoclassical flux,

$$\langle n_a \mathbf{V}_a \cdot \nabla \psi \rangle_{nc} = \frac{1}{e_a p'} \langle J_{\parallel} F_{a\parallel} + \boldsymbol{\pi} : \nabla \mathbf{J} \rangle \quad (35)$$

where the viscosity tensor is $\boldsymbol{\pi}_a = (p_{\parallel} - p_{\perp})(\mathbf{b}\mathbf{b} - \mathbf{I}/3)$. The first term in (35) is proportional to ν and therefore dominates at high collisionality, but vanishes when there is only a single ion species because of momentum conservation in like-particle collisions. All that remains is therefore the particle flux caused by parallel viscosity, which is inversely proportional to ν at high collisionality [31]. In the pure pitch-angle-scattering model however, parallel momentum conservation is violated, leading to spurious friction-driven transport proportional to ν . This is why the green curves have a slope of +1 for large ν in the logarithmic plots of L_{11} and L_{12} in Figures (4)-(5), while the blue and red curves have the slope -1.

A similar difference between the momentum-conserving and pitch-angle-scattering operators is evident in the parallel conductivity coefficient L_{33} . The flow that arises in response to a parallel electric field is determined by the parallel momentum equation

$$n_a Z_a e E_{\parallel} = \mathbf{b} \cdot \nabla p_a + \mathbf{b} \cdot (\nabla \cdot \boldsymbol{\pi}_a) + F_{a\parallel}, \quad (36)$$

where the parallel friction force $F_{\parallel a}$ again vanishes when only a single ion species is considered. Hence

$$n_a Z_a e \langle B E_{\parallel} \rangle = \langle \mathbf{B} \cdot (\nabla \cdot \boldsymbol{\pi}_a) \rangle = \langle (p_{\perp} - p_{\parallel}) \nabla_{\parallel} B \rangle. \quad (37)$$

In the absence of radial gradients, the pressure anisotropy in the Pfirsch-Schlüter regime is proportional to the parallel flow velocity and inversely proportional to the collision frequency [43]. The flow $\langle V_{\parallel} B \rangle$ is therefore proportional to ν in the Pfirsch-Schlüter regime unless momentum conservation is violated. In the latter case, the spurious friction force causes $\langle V_{\parallel} B \rangle$ to be inversely proportional to ν , as can be seen in Figs. (4)-(5).

When $\nu' < 1$, the resolution required in the θ , ζ , and ξ coordinates increases as ν' decreases, due to the boundary layers that develop in phase space. The highest resolution used for results presented here, corresponding to the W7-X calculations at $\nu' = 10^{-3}$, was $N_{\theta} = 29$, $N_{\zeta} = 83$, $N_{\xi} = 180$, and $N_x = 5$, giving a $2,166,302 \times 2,166,302$ linear system. Here, N_j is the number of grid points or modes in coordinate j . Each calculation at this resolution with the Fokker-Planck collision operator required $\sim 30 - 50$ minutes to run on 4 nodes of the Edison computer at NERSC. At higher collisionality, lower resolution is sufficient, so memory and time requirements are reduced; computations with $\nu' > 10^{-2}$ can typically be run on a laptop.

In the short-mean-free-path limit $\nu' \gg 1$, the ion transport and flow can be computed analytically in terms of the parallel current [43]. The transport matrix elements associated with the Fokker-Planck collision operator may therefore be extracted from Ref. [43] and are summarized in Appendix B. Plotted in figures 4 and 5 (red dashed lines), these analytic high-collisionality limits agree quite well with the Fokker-Planck SFINCS computations in the appropriate $\nu' \gg 1$ limit.

At any collisionality, when the pure pitch-angle scattering collision operator and DKES trajectories are chosen, the kinetic equation solved in SFINCS becomes identical to the one solved in the DKES code [5, 6]. In this case, it was verified that the two codes agreed for all elements of the transport matrix, as demonstrated in figure 5. For this figure, the monoenergetic transport coefficients computed by DKES have been integrated over velocity with the appropriate weights and normalized in the same way as (30).

VIII. DISCUSSION AND CONCLUSIONS

Different stellarator transport codes make different assumptions about the details of the drift-kinetic equation, and our goal in this work has been to examine the consequences of these details. In this work, we have compared three versions of the drift-kinetic equation for

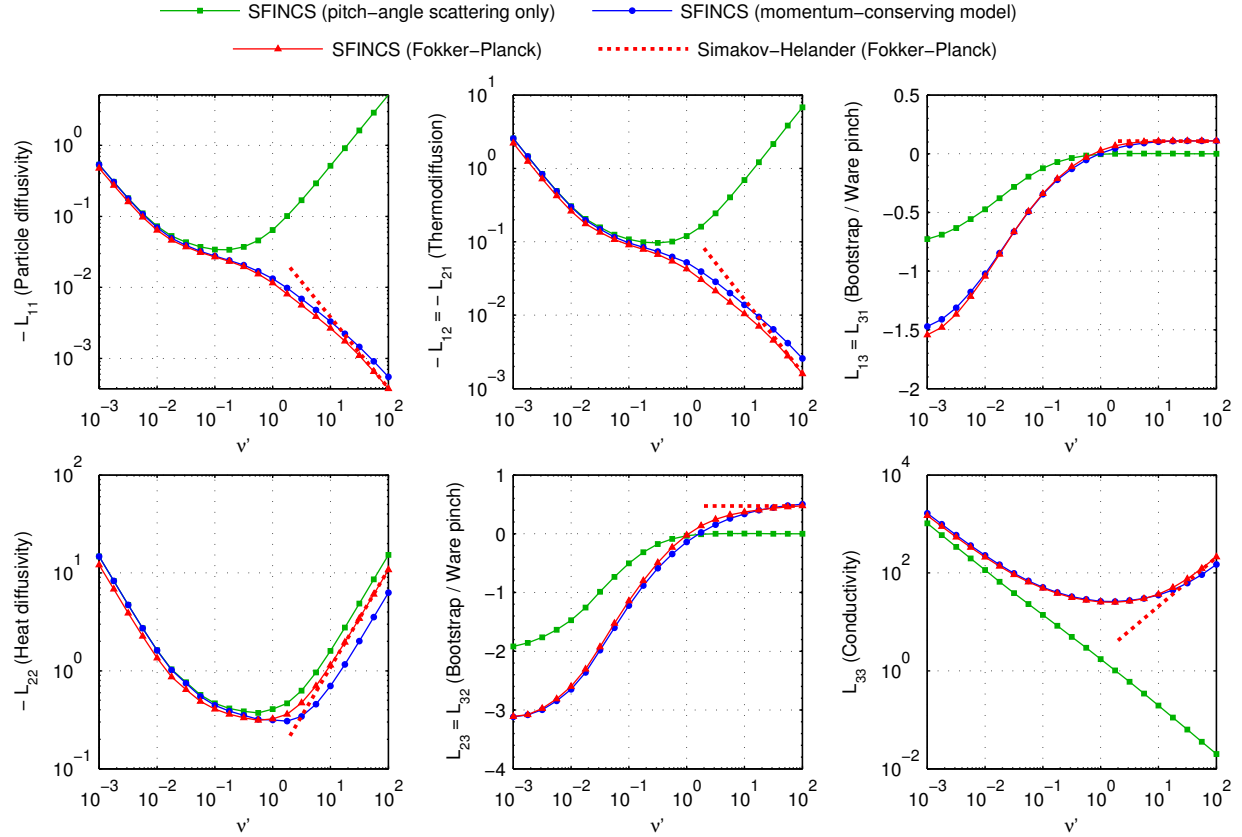


FIG. 4: (Color online) The ion transport matrix elements (defined in (30)) are plotted as functions of the collisionality (31) for LHD geometry at $E_r = 0$. SFINCS computations for three different collision operators are compared. Dashed red lines indicate the analytic high-collisionality limits for Fokker-Planck collisions, discussed in appendix B and in Ref. [43], which agree quite well with the SFINCS Fokker-Planck computations at high collisionality.

a stellarator, consisting of (15) with the coefficients (16), (17), or (18). These three sets of expressions for $\dot{\mathbf{r}}_a$, \dot{x}_a , and $\dot{\xi}_a$ may be interpreted as effective particle trajectories (although we solve each form of the kinetic equation using continuum numerical methods). At first glance, (16) and (18) appear more accurate than (17). However, as we have shown in section III, the kinetic equation (15) with (16) or (18) is not well behaved when $E_r \neq 0$, with an unphysical constraint forced upon the distribution function. This analytic property of the kinetic equation must be dealt with before attempting to solve the equation numerically.

To eliminate this problem of unphysical constraints, we propose formulating the kinetic problem as in (26) with (25). A particle and heat source are introduced, along with the additional constraints that all the flux-surface-averaged density and pressure reside in the

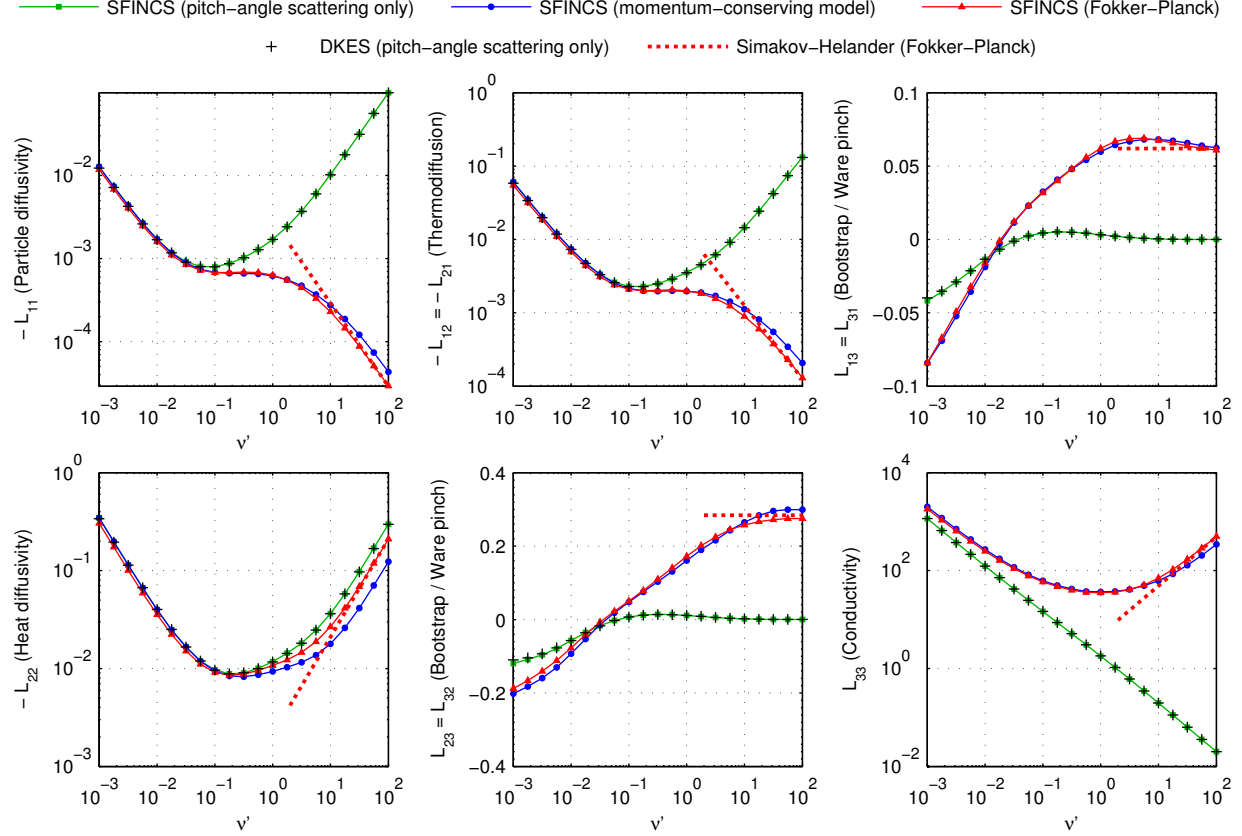


FIG. 5: (Color online) The ion transport matrix elements (defined in (30)) are plotted as functions of the collisionality (31) for LHD geometry at $E_r = 0$. SFINCS computations for three different collision operators are compared. Dashed red lines indicate the analytic high-collisionality limits for Fokker-Planck collisions, discussed in appendix B and in Ref. [43], which agree quite well with the SFINCS Fokker-Planck computations at high collisionality. Also shown (black crosses) are the transport matrix elements computed using the DKES code [5, 6], which uses a pitch-angle scattering collision operator, demonstrating excellent agreement with SFINCS when the latter is run with the same collision model.

leading-order Maxwellian. For the model (17), the sources always vanish. For the model (16), the particle source vanishes for any E_r , and the energy source vanishes when E_r takes on its ambipolar value. The equations (26) have been implemented in a new time-independent continuum code SFINCS, and the resulting ion transport matrices have been compared for the geometries of the LHD and W7-X stellarators. When E_r is below roughly one-third of the resonant value, the three models give nearly indistinguishable results. This finding

confirms that the incompressible- $\mathbf{E} \times \mathbf{B}$ trajectory model used in some codes [5, 6] is quite accurate in this small- E_r regime, which is typically satisfied in experiments. Physically, the effect of E_r in this regime is to generate a $\sqrt{\nu}$ regime of transport due to poloidal precession of helically trapped particles, and this process is retained (at least approximately) in all three trajectory models. Once E_r approaches the resonance, however, the three trajectory models yield substantially different results. This $E_r \sim E_r^{\text{res}}$ regime can be relevant to experiments with high ratios T_e/T_i [23, 45] and strong gradients [46]. In figure 3, we find that in the large- E_r region anticipated for the edge of W7-X, the bootstrap current density in the full trajectory model is modestly reduced (by 8%) compared to an incompressible- $\mathbf{E} \times \mathbf{B}$ calculation, but should larger values of E_* arise, we expect the deviation could grow more significant.

Since full coupling in the speed coordinate x_a is retained in our numerical implementation, it is possible to directly compare results from the full linearized Fokker-Planck collision operator to results from simpler collision models. At low collisionality, the ion transport matrix elements L_{11} , L_{12} , L_{21} , and L_{22} are nearly identical for the three collision models considered. This result makes sense physically since these matrix elements at low collisionality are associated with a piece of the distribution function that is localized to a narrow range of pitch angles, so pitch angle diffusion is the dominant collisional process. However, these same matrix elements at higher collisionality, or the other matrix elements at any collisionality, are sensitive to momentum conservation. The momentum-conserving model operator results in the correct scaling with collisionality when compared to the full linearized Fokker-Planck operator. However, there are still $O(1)$ differences in the transport coefficients computed with these two collision operators.

Acknowledgments

This work was supported by the US Department of Energy through grants DE-FG02-91ER-54109 and DE-FG02-93ER-54197. M. L. is grateful to the Plasma Science and Fusion Center at the Massachusetts Institute of Technology, where he carried out much of the code development, and for travel support from the Max-Planck-Institut für Plasmaphysik in Greifswald, Germany. Some of the computer simulations presented here used resources of the National Energy Research Scientific Computing Center (NERSC), which is supported

by the Office of Science of the U.S. Department of Energy under Contract No. DE-AC02-05CH11231. M. L. was supported by the Fusion Energy Postdoctoral Research Program administered by the Oak Ridge Institute for Science and Education. We are thankful to J. Geiger for providing the W7-X equilibrium data, and to Craig Beidler, Albert Mollén, and Peter Catto for other input on this work.

APPENDIX A: QUASISYMMETRY ISOMORPHISM

A useful test of a stellarator neoclassical code such as the one described here is the quasisymmetry isomorphism, discussed analytically in Refs. [47–49]. In this test, the magnetic field is specified as $B(\theta, \zeta) = y(M\theta - N\zeta)$ for some given periodic function y and integers M and N . The kinetic equation is solved for several values of M and N , varying the collision frequency with each run so that $\nu_{ii}/|M - N/\iota|$ remains fixed. As M and N are varied, G , I , ι , $dn/d\psi$, $dT/d\psi$, and other input quantities are also kept fixed. Under these circumstances, it is known analytically [47–49] that the flow and heat flux should obey the transformations

$$\langle V_{\parallel} B \rangle \frac{M - N/\iota}{NI + MG} = C_V \quad (\text{A1})$$

and

$$\left\langle \int d^3v f_{i1} \frac{v^2}{2} \mathbf{v}_{mi} \cdot \nabla \psi \right\rangle \frac{|M - N/\iota|}{(NI + MG)^2} = C_q \quad (\text{A2})$$

respectively, where the quantities C_V and C_q should be independent of M and N . It was verified that the SFINCS code obeyed these isomorphism transformations for a range of y , collisionality regimes, and collision operators.

APPENDIX B: ION TRANSPORT MATRIX AT HIGH COLLISIONALITY

From the analytic calculations presented in Ref. [43] we can derive expressions for L_{jk} of Eq. (30) in the Pfirsch-Schlüter regime. The transport matrix elements then depend on the function u given by the solution to Eq. (8) in Ref. [43]; u is proportional to the parallel current divided by B . All coefficients but L_{33} are straightforwardly obtained from Eqs. (14), (18) and (26) in Ref. [43] for the radial ion heat flux, the parallel ion flow, and the radial current respectively, by suitable choices of the thermodynamic forces in the right-hand-side of Eq. (30) and using the symmetry of the transport matrix. To find the

parallel conductivity coefficient L_{33} we substitute the pressure anisotropy, given by Eq. (20) in Ref. [43], into Eq. (37) (of this paper) in the absence of radial gradients (i.e. when E_{\parallel} is the only thermodynamic force present). Then L_{33} can be found from the flow $\langle V_{\parallel} B \rangle$.

Expressions for the matrix coefficients in the Pfirsch-Schlüter regime are summarized in Eqs. (B1)-(B2). Three numerical coefficients in the function $K_2^{\text{Simakov}}(\psi)$ arise from generalized Spitzer problems, which were solved in Ref. [43] by keeping a small number of Laguerre polynomials in kinetic energy. When these generalized Spitzer problems are solved numerically keeping many more energy polynomials, we obtain the more accurate coefficients given in K_2 below.

$$\begin{aligned}
L_{11} &= 0.96 \cdot 2^{1/2} \cdot \frac{3}{4} \frac{(G + \iota I)^2}{\iota^2 G^2} G_1(\psi) \frac{1}{\nu'}, \\
L_{12} = L_{21} &= 0.96 \cdot 2^{1/2} \frac{(G + \iota I)^2}{\iota^2 G^2} [3.245 G_1(\psi) + 0.085 G_2(\psi)] \frac{1}{\nu'}, \\
L_{13} = L_{31} &= \frac{\langle u B^2 \rangle}{G \iota} - \frac{\langle B^2 \rangle}{G \iota} K_1(\psi), \\
L_{22} &= 2^{1/2} \cdot \frac{8}{5} \frac{1}{\iota^2 G^2} B_0^2 H(\psi) \nu', \\
L_{23} = L_{32} &= \frac{1}{\iota G} \left[\frac{5}{2} \langle u B^2 \rangle - \frac{5}{2} K_1(\psi) \langle B^2 \rangle + K_2(\psi) \langle B^2 \rangle \right], \\
L_{33} &= \frac{1}{3 \cdot 0.96 \cdot 2^{1/2}} \frac{1}{(G + \iota I)^2} \frac{\langle B^2 \rangle^2}{\langle (\nabla_{\parallel} B)^2 \rangle} \nu',
\end{aligned} \tag{B1}$$

$$\begin{aligned}
G_1(\psi) &= \frac{\langle (\nabla_{\parallel} \ln B) \nabla_{\parallel} (uB^2) \rangle^2}{\langle (\nabla_{\parallel} B)^2 \rangle} - \left\langle \left[\frac{\nabla_{\parallel} (uB^2)}{B} \right]^2 \right\rangle, \\
G_2(\psi) &= \langle u (\nabla_{\parallel} \ln B) \nabla_{\parallel} (uB^2) \rangle - \frac{\langle (\nabla_{\parallel} \ln B) \nabla_{\parallel} (uB^2) \rangle \langle u (\nabla_{\parallel} B)^2 \rangle}{\langle (\nabla_{\parallel} B)^2 \rangle}, \\
K_1(\psi) &= \frac{\langle (\nabla_{\parallel} \ln B) \nabla_{\parallel} (uB^2) \rangle}{2 \langle (\nabla_{\parallel} B)^2 \rangle}, \\
K_2(\psi) &= 1.97213 \frac{\langle uB^2 \rangle}{\langle B^2 \rangle} - 1.03287 \cdot 2K_1(\psi) + 0.09361 \frac{\langle u (\nabla_{\parallel} B)^2 \rangle}{\langle (\nabla_{\parallel} B)^2 \rangle}, \\
K_2^{\text{Simakov}}(\psi) &= 1.77 \frac{\langle uB^2 \rangle}{\langle B^2 \rangle} - 0.91 \cdot 2K_1(\psi) + 0.05 \frac{\langle u (\nabla_{\parallel} B)^2 \rangle}{\langle (\nabla_{\parallel} B)^2 \rangle}, \\
H(\psi) &= \frac{\langle uB^2 \rangle^2}{\langle B^2 \rangle} - \langle u^2 B^2 \rangle.
\end{aligned} \tag{B2}$$

-
- [1] G. Kagan and P. J. Catto, Plasma Phys. Controlled Fusion **52**, 055004 (2010).
- [2] A. A. Galeev, R. Z. Sagdeev, H. P. Furth, and M. N. Rosenbluth, Phys. Rev. Lett. **22**, 511 (1969).
- [3] D. D.-M. Ho and R. M. Kulsrud, Phys. Fluids **30**, 442 (1987).
- [4] C. D. Beidler, K. Allmaier, M. Y. Isaev, S. V. Kasilov, W. Kernbichler, G. O. Leitold, H. Maassberg, D. R. Mikkelsen, S. Murakami, M. Schmidt, D. A. Spong, V. Tribaldos, and A. Wakasa, Nucl. Fusion **51**, 076001 (2011).
- [5] S. P. Hirshman, K. C. Shaing, W. I. van Rij, C. O. Beasley Jr., and E. C. Crume Jr., Phys. Fluids **29**, 2951 (1986).
- [6] W. I. van Rij and S. P. Hirshman, Phys. Fluids B **3**, 563 (1989).
- [7] C. D. Beidler and W. D. D'haeseleer, Plasma Phys. Controlled Fusion **37**, 463 (1995).
- [8] V. Tribaldos, Phys. Plasmas **8**, 1229 (2001).
- [9] D. A. Spong, Phys. Plasmas **12**, 056114 (2005).
- [10] W. Kernbichler, S. V. Kasilov, G. O. Leitold, V. V. Nemov, and K. A. K, 33rd EPS Conference on Plasma Phys., Rome **30I**, P (2006).

- [11] S. Satake, R. Kanno, and H. Sugama, Plasma Fusion Res. **3**, S1062 (2008).
- [12] S. Satake, Y. Idomura, H. Sugama, and T.-H. Watanabe, Comp. Phys. Comm. **181**, 1069 (2010).
- [13] J. M. García-Regaña, R. Kleiber, C. D. Beidler, Y. Turkin, H. Maassberg, and P. Helander, Plasma Phys. Controlled Fusion **55**, 074008 (2013).
- [14] P. Helander, Phys. Plasmas **14**, 104501 (2007).
- [15] H. Sugama, T. H. Watanabe, M. Nunami, and S. Nishimura, Plasma Phys. Controlled Fusion **53**, 024004 (2011).
- [16] C. D. Beidler, M. Y. Isaev, S. V. Kasilov, W. Kernbichler, H. Maassberg, S. Murakami, V. V. Nemov, and D. A. S. V. Tribaldos, Proceedings of the 17th International Toki Conference and 16th International Stellarator/Heliotron Workshop, Toki (2007).
- [17] M Landreman, Plasma Phys. Controlled Fusion **53**, 082003 (2011).
- [18] O. Sauter, R. W. Harvey, and F. L. Hinton, Comp. Phys. Comm. **34**, 169 (1994).
- [19] O. Sauter, C. Angioni, and Y. R. Lin-Liu, Phys. Plasmas **6**, 2834 (1999).
- [20] S. K. Wong and V. S. Chan, Plasma Phys. Controlled Fusion **53**, 095005 (2011).
- [21] E. A. Belli and J. Candy, Plasma Phys. Controlled Fusion **54**, 015015 (2012).
- [22] M. Landreman and D. R. Ernst, J. Comp. Phys. **243**, 130 (2013).
- [23] A. Briesemeister, K. Zhai, D. T. Anderson, F. S. B. Anderson, and J. N. Talmadge, Plasma Phys. Controlled Fusion **55**, 014002 (2013).
- [24] M. Taguchi, Phys. Fluids B **4**, 3638 (1992).
- [25] H. Sugama and S. Nishimura, Phys. Plasmas **9**, 4637 (2002).
- [26] H. Maassberg, C. D. Beidler, and Y. Turkin, Phys. Plasmas **16**, 072504 (2009).
- [27] R. D. Hazeltine, Plasma Phys. **15**, 77 (1973).
- [28] M. Landreman and D. R. Ernst, Plasma Phys. Controlled Fusion **54**, 115006 (2012).
- [29] M. Landreman and P. J. Catto, Plasma Phys. Controlled Fusion **55**, 095017 (2013).
- [30] M. N. Rosenbluth, W. M. MacDonald, and D. L. Judd, Phys. Rev. **107**, 1 (1957).
- [31] P. Helander and D. J. Sigmar, *Collisional Transport in Magnetized Plasmas* (Cambridge University Press, Cambridge, 2002).
- [32] M. Landreman, F. I. Parra, P. J. Catto, D. R. Ernst, and I. Pusztai, arXiv:1312.2148 (2013).
- [33] S. Balay, J. Brown, K. Buschelman, W. D. Gropp, D. Kaushik, M. G. Knepley, L. C. McInnes, B. F. Smith, and H. Zhang, “PETSc Web page,” (Accessed October 6, 2012),

- <http://www.mcs.anl.gov/petsc>.
- [34] S. Balay, J. Brown, , K. Buschelman, V. Eijkhout, W. D. Gropp, D. Kaushik, M. G. Knepley, L. C. McInnes, B. F. Smith, and H. Zhang, “PETSc users manual,” Tech. Rep. ANL-95/11 - Revision 3.3 (Argonne National Laboratory, 2012).
 - [35] Y. Saad and M. H. Schultz, SIAM J. Sci. and Stat. Comput. **7**, 856 (1986).
 - [36] G. L. G. Sleijpen and D. R. Fokkema, Electr. Trans. Num. Anal. **1**, 11 (1993).
 - [37] X. Li, J. Demmel, J. Gilbert, L. Grigori, M. Shao, and I. Yamazaki, “SuperLU Users’ Guide,” Tech. Rep. LBNL-44289 (Lawrence Berkeley National Laboratory, 1999) <http://crd.lbl.gov/~xiaoye/SuperLU/>. Last update: August 2011.
 - [38] X. S. Li and J. W. Demmel, ACM Trans. Mathematical Software **29**, 110 (2003).
 - [39] A. Iiyoshi, M. Fujiwara, O. Motojima, N. Ohyabu, and K. Yamazaki, Fusion Tech. **17**, 169 (1990).
 - [40] C. D. Beidler, G. Grieger, F. Herrnegger, W. Harmeyer, J. Kisslinger, W. Lotz, H. Maassberg, P. Merkel, J. Nührenberg, F. Rau, J. Sapper, F. Sardei, R. Scardovelli, A. Schlüter, and H. Wobig, Fusion Tech. **17**, 148 (1990).
 - [41] G. Grieger, C. D. Beidler, E. Harmeyer, W. Lotz, J. Kisslinger, P. Merkel, J. Nührenberg, F. Rau, E. Strumberger, and H. Wobig, Fusion Tech. **21**, 1767 (1992).
 - [42] Y. Turkin, C. D. Beidler, H. Maassberg, S. Murakami, V. Tribalos, and A. Wakasa, Phys. Plasmas **18**, 022505 (2011).
 - [43] A. N. Simakov and P. Helander, Phys. Plasmas **16**, 042503 (2009).
 - [44] S. Braun and P. Helander, Phys. Plasmas **17**, 072514 (2010).
 - [45] J. Lore, W. Guttenfelder, A. Briesemeister, D. T. Anderson, F. S. B. Anderson, C. B. Deng, K. M. Likin, D. A. Spong, J. N. Talmadge, and K. Zhai, Phys. Plasmas **17**, 056101 (2010).
 - [46] J. Baldzuhn, M. Kick, H. Maassberg, and the W7-AS Team, Plasma Phys. Controlled Fusion **40**, 967 (1998).
 - [47] A. Pytte and A. H. Boozer, Phys. Fluids **24**, 88 (1981).
 - [48] A. H. Boozer, Phys. Fluids **26**, 496 (1983).
 - [49] M. Landreman and P. J. Catto, Plasma Phys. Controlled Fusion **53**, 015004 (2011).